

Unveiling the Spectral Morphological Division of Fast Radio Bursts with CHIME/FRB Catalog 2

WAN-PENG SUN ,¹ YIN-LONG CAO ,¹ YONG-KUN ZHANG ,² JI-GUO ZHANG ,¹ XIAOHUI LIU ,^{2,3} YICHAO LI ,¹
 FU-WEN ZHANG ,⁴ WAN-TING HOU ,⁵ JING-FEI ZHANG ,¹ AND XIN ZHANG ,^{1,6,7}

¹*Liaoning Key Laboratory of Cosmology and Astrophysics, College of Sciences, Northeastern University, Shenyang 110819, China*

²*National Astronomical Observatories, Chinese Academy of Sciences, Beijing 100101, China*

³*School of Astronomy and Space Science, University of Chinese Academy of Sciences, Beijing 100049, China*

⁴*College of Science, Guilin University of Technology, Guilin 541004, China*

⁵*College of Mathematics and Statistics, Liaoning University, Shenyang 110036, China*

⁶*MOE Key Laboratory of Data Analytics and Optimization for Smart Industry, Northeastern University, Shenyang 110819, China*

⁷*National Frontiers Science Center for Industrial Intelligence and Systems Optimization, Northeastern University, Shenyang 110819, China*

ABSTRACT

Fast radio bursts (FRBs) are commonly divided into repeating and apparently non-repeating sources, but whether these represent distinct physical populations remains uncertain. In this work, we apply an unsupervised machine learning methods combining Uniform Manifold Approximation and Projection (UMAP) with density-based clustering to analyze CHIME/FRB Catalog 2. We find that FRBs remain primarily separated into two clusters in the multi-dimensional parameter space, with a recall of 0.94 for known repeaters, indicating strong robustness. Consistent with Catalog 1 analyses, we confirm that the spectral morphology parameter, specifically spectral running remains the key discriminator between the two populations, indicating that narrowband emission is an intrinsic and persistent property of repeating FRBs. With the enlarged Catalog 2 sample, we further identify a stable subclass of atypical repeaters (about 6% of repeating bursts) that are broadband, shorter in duration, and more luminous, resembling non-repeating bursts. The Nonrepeater-like cluster also shows higher inferred energies and dispersion measures, consistent with a scenario in which apparently non-repeating FRBs may result from observational incompleteness, with low-energy repeating bursts remaining undetected. Our results provide new statistical evidence for a physical connection between repeating and non-repeating FRBs.

Keywords: Radio transient sources (2008) — Radio bursts (1339) — Classification systems (253)

1. INTRODUCTION

Fast Radio Bursts (FRBs) are millisecond-duration, extremely energetic radio transients. Since their discovery in 2007 (Lorimer et al. 2007), their extreme energetics and possible cosmological origins have made them one of the most active frontiers in astrophysics, although their physical origin has not yet been fully understood. Observationally, most FRBs exhibit dispersion measures (DMs) well in excess of the maximum Galactic contribution, indicating that they predominantly arise from compact sources at cosmological distances (Thornton et al. 2013; Spitler et al. 2014; Tendulkar

et al. 2017; Marcote et al. 2017; Petroff et al. 2022; Zhang 2023, 2024). The burst from the Galactic magnetar SGR 1935+2154 (Bochenek et al. 2020; CHIME/FRB Collaboration et al. 2020), however, has demonstrated that magnetars can account for at least a fraction of the population. Owing to their large DMs, high brightness, and cosmological distances, FRBs have gradually emerged as powerful probes of the intergalactic medium and the cosmic matter distribution (Macquart et al. 2020; Zhao et al. 2020; Zhang et al. 2023, 2025a,b). Over the past decade, FRB observations have revealed diverse activity: some sources produce multiple bursts (repeaters), whereas others have only been detected once (non-repeaters). Whether this distinction reflects intrinsically different progenitors or is instead driven by observational incompleteness and selection biases remains one of the most debated questions in current FRB research (Zhang 2023).

Corresponding author: Yichao Li
 liyichao@mail.neu.edu.cn

Corresponding author: Xin Zhang
 zhangxin@mail.neu.edu.cn

Analyzing the observational characteristics of repeating and non-repeating FRBs is a key approach to understanding their physical origins. Early studies noted that repeating FRBs tend to exhibit more complex temporal structures, longer pulse widths, and relatively narrower spectra (Pleunis et al. 2021; Kumar et al. 2021; CHIME/FRB Collaboration et al. 2023), whereas non-repeating sources are typically short-duration, broadband bursts (CHIME/FRB Collaboration et al. 2021; Pleunis et al. 2021; Cui et al. 2021; Zhang et al. 2022). Sun’s analysis based on the first CHIME/FRB sample further revealed that the most significant differences between the two classes lie in their spectral shape parameters, particularly the spectral running (Sun et al. 2025a), indicating that repeaters generally have steeper, narrower spectra, while non-repeaters tend to show flatter and broader spectra. These systematic differences were robustly confirmed in the analysis of the larger CHIME/FRB Catalog 2 sample (Catalog 2) (FRB Collaboration et al. 2026). Nevertheless, these distinctions are not absolute, as a small fraction of repeating bursts display spectral and pulse-duration properties highly similar to those of typical broadband, short-duration non-repeating bursts (FRB Collaboration et al. 2026).

Notably, statistical studies of the burst rates for the two classes show that, after correcting for observational duration and detection efficiency, their distributions do not exhibit a bimodal structure (CHIME/FRB Collaboration et al. (2023)). This suggests that repeaters and non-repeaters may not constitute entirely distinct populations, and that non-repeating FRBs could potentially repeat on longer timescales. In particular, Sun et al. (2025b) found that, in the γ - r parameter space, the burst rate correlates positively with pulse width and negatively with spectral bandwidth, lending strong support to the single-progenitor scenario proposed by (CHIME/FRB Collaboration et al. (2023)). Furthermore, no significant differences have yet been found in the host galaxy properties of the two classes (Ma et al. 2025; CHIME/FRB Collaboration et al. 2025; Pastor-Marazuela et al. 2026), and analyses of their energy distributions indicate that non-repeating FRBs may simply represent the rare, high-energy tail of the repeating population (Kirsten et al. 2024; Ould-Boukattine et al. 2024). Collectively, these findings highlight the complexity of the FRB dichotomy and underscore the need to reassess classification in a higher-dimensional, multi-parameter observational space.

In recent years, machine learning has demonstrated unique advantages in the classification of FRBs. Unsupervised methods can perform dimensionality reduction and clustering on multi-dimensional observational parameters without relying on prior labels, thereby revealing the natural clustering and structural differences between repeating and non-repeating FRBs in parameter space (Chen et al. 2022; Yang et al. 2023; Zhu-Ge et al. 2023; García et al. 2024; Sun et al. 2025a;

Qiang et al. 2025; Liu et al. 2025; Madheshwaran et al. 2025; Júnior et al. 2026). On the other hand, supervised methods leverage information from known repeating FRBs to establish nonlinear mappings between input features and classes in high-dimensional feature spaces (Luo et al. 2023; Sharma & Rajpaul 2024; Kharel et al. 2025; Kharel et al. 2025; Arni et al. 2025), enabling the prediction of potential repeating candidates. Compared to supervised approaches, unsupervised methods are more model-independent and do not require prior training, making them particularly well suited for uncovering statistical correlations among multi-dimensional FRB observables. Our previous work (Sun et al. 2025a) demonstrated that the spectral shape parameters r and γ , which are closely related to FRB spectral morphology, serve as the key features for distinguishing repeaters from non-repeaters, achieving maximal separation between the two classes. Similar conclusions have been independently confirmed in recent studies (Kharel et al. 2025; Arni et al. 2025).

Although unsupervised methods have demonstrated distinct advantages, their effectiveness largely depends on sample size and the completeness of the feature space. Previous studies, often based on early samples such as CHIME/FRB Catalog 1, were limited by the number of sources and statistical coverage, making it difficult to fully characterize rare but potentially physically meaningful events in parameter space, particularly the uncommon repeaters exhibiting broadband emission. With the release of Catalog 2, the FRB sample size has increased by an order of magnitude. This not only provides a crucial opportunity to test the robustness of previous statistical conclusions under large-sample conditions, but also allows for systematic statistical analyses of rare repeating bursts that were previously sparsely represented. Motivated by this, the present study employs unsupervised machine learning on the large Catalog 2 sample, using multi-dimensional observational parameters to re-examine the classification of repeating and non-repeating FRBs. We focus not only on the distinguishing features of the two classes in a global statistical sense, but also on the statistical differences and connections among distinct subclass within the repeating population, thereby providing new statistical insight into the physical origins of FRBs.

The structure of our paper is as follows: In Section 2, we describe the data set from Catalog 2 used in this study, along with the implementation of the UMAP algorithm and its parameter settings. In Section 3, we present the UMAP clustering results for repeating and non-repeating FRBs from Catalog 2, along with a detailed comparison of parameter distributions for the reclassified sources and an analysis of the distinctions between typical and atypical repeaters. A brief summary and discussion are provided in Section 4. In this work, we adopt the cosmological parameters $H_0 = 67.66$ km

$\text{s}^{-1} \text{Mpc}^{-1}$, $\Omega_b = 0.04897$, $\Omega_m = 0.3111$, and $\Omega_\Lambda = 0.6874$ from the Planck 2018 results (Aghanim et al. 2020).

2. DATA AND ALGORITHM PARAMETERS

2.1. Data Sample Selection

This study employs the latest and currently largest FRB dataset released by the CHIME/FRB project, the second Catalog 2 (FRB Collaboration et al. 2026). All events were detected by the same instrument operating in the 400-800 MHz band under uniform observational conditions, yielding a highly homogeneous sample of FRB events. Such a consistent and statistically rich dataset provides an unprecedented foundation for large-scale population studies. Catalog 2 covers 4539 FRBs detected between 2018 July 25 and 2023 September 15 (FRB Collaboration et al. 2026). We exclude 518 events that lack flux measurements. In addition, many FRBs exhibit complex temporal and spectral morphology and can be decomposed into multiple sub-bursts, which appear as distinct peaks in the dynamic spectrum (Sheikh et al. 2024; Brown et al. 2024). Since these sub-components often differ in spectral properties, we treat each sub-burst as an independent entry in our analysis. Our final dataset includes 4527 FRBs in total, consisting of 3373 non-repeaters and 1154 repeaters originating from 83 distinct repeating sources.

2.2. FRB Feature Parameters

In our previous work (Sun et al. 2025a,b), we provided a detailed description of the characteristic parameters that reflect the intrinsic emission properties and spectral characteristics of FRBs, which are capable of distinguishing between repeating and non-repeating FRBs. Our goal was to identify the most critical and minimal set of parameters needed to differentiate repeating FRBs from non-repeating ones. To achieve this, we selected a small number of directly observed parameters and applied machine-learning classification techniques for the analysis. The chosen parameters include flux density (S_ν), fluence (F_ν), sub-burst pulse width (Δt_{ws}), spectral index (γ), spectral running (r), the lowest frequency (ν_{Low}), the highest frequency (ν_{High}), and peak frequency (ν_{Peak}). These parameters have been shown to be effective for distinguishing repeaters from non-repeaters when used with machine learning techniques. In this study, we select these eight parameters for the Catalog 2. A detailed description of these parameters can be found in FRB Collaboration et al. (2026).

2.3. UMAP Algorithm

To investigate potential patterns and similarity structures of FRBs in the multi-dimensional parameter space, we employ the Uniform Manifold Approximation and Projection (UMAP) algorithm (McInnes et al. 2018; Becht et al. 2019). As a nonlinear dimensionality-reduction technique grounded in Riemannian geometry and algebraic topology,

UMAP assumes that the data is uniformly distributed on a locally connected manifold. The algorithm constructs a high-dimensional fuzzy topological representation and optimizes the low-dimensional embedding by minimizing the cross-entropy between the high-dimensional and low-dimensional topological graphs. A distinct advantage of UMAP over similar methods is its superior computational efficiency on large datasets and its ability to preserve the global structure of the data more effectively while simultaneously maintaining local neighborhood relationships, making it highly suitable for uncovering meaningful substructures or clustering tendencies within complex astrophysical datasets.

The topology of the resulting embedding is primarily governed by two key hyperparameters: `n_neighbors` and `min_dist`. The `n_neighbors` parameter determines the size of the local neighborhood used to approximate the manifold structure, it serves a role analogous to perplexity in t-SNE, balancing the emphasis between fine local details and the broader global structure. The `min_dist` parameter controls the minimum separation distance between points in the low-dimensional space. Lower values allow points to clump tightly together, potentially revealing denser substructures, whereas higher values enforce a more dispersed distribution, which aids in visualizing the continuous topological structure. Throughout this analysis, we adopt `n_neighbors` = 15 for the UMAP dimensionality reduction. The parameter `min_dist` is set to 0.1. We found that this default value, combined with the chosen neighborhood size, effectively balances the preservation of local fine structure and global topology. Other hyperparameters are kept at their default values as specified in the `umap-learn` library. Proper tuning of these parameters is crucial for generating a stable and physically interpretable embedding. Further details on UMAP implementation and parameter tuning can be found in the official documentation¹.

3. RESULTS AND DISCUSSION

3.1. UMAP Results

To visualize the distribution of 4527 FRBs in the multidimensional parameter space, we apply UMAP to the sample, and the result is shown in Figure 1. In this embedding space, red dots represent confirmed repeaters, while blue dots denote events that have not yet shown repetition observationally. Consistent with the foundational patterns identified in Sun et al. (2025a,b), the enlarged sample still exhibits a bimodal structure. As illustrated, most confirmed repeaters are densely concentrated on the lower-right side. In contrast, the distribution of apparent non-repeaters is more complex: while a significant portion forms a distinct, isolated cluster in the upper-left region, others are widely distributed and show

¹ <https://umap-learn.readthedocs.io/>

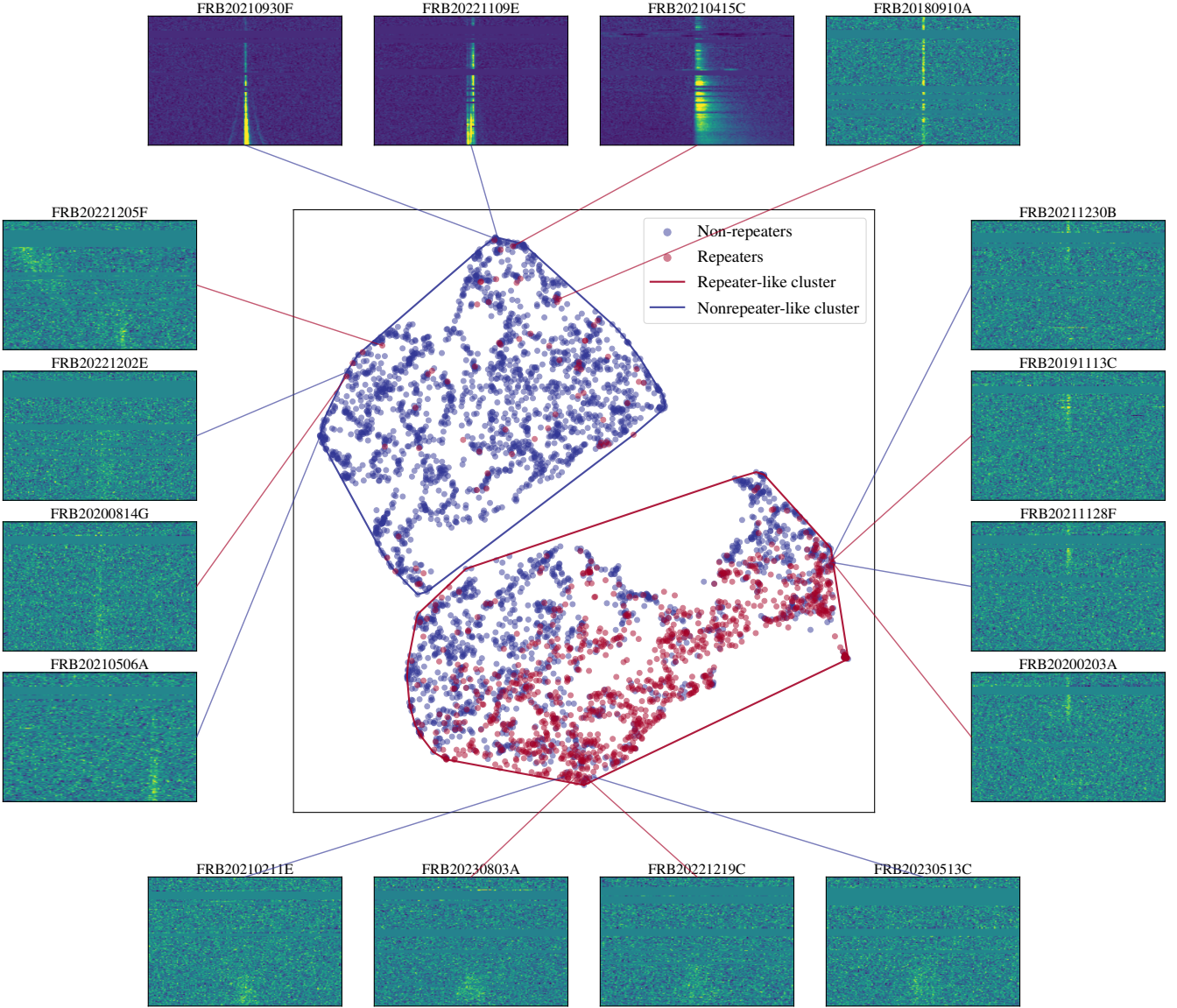


Figure 1. The embedding space of the UMAP dimension reduction results of the Catalog 2. The blue dots represent the non-repeaters and the red dots are repeaters. The blue and red contours indicate the clusters identified by HDBSCAN, corresponding to the Nonrepeater-like cluster and Repeater-like cluster, respectively. The surrounding panels display the dynamic spectra for representative FRBs selected from both clusters.

substantial spatial overlap with the primary repeaters in the lower-right. It is worth noting that, in the upper-left region of the embedding space, a subset of repeaters now appears within areas dominated by non-repeaters, which constitutes the most notable change relative to earlier results derived from the smaller CHIME/FRB Catalog 1 sample.

It should be noted that the UMAP axes themselves do not carry direct physical meaning, and distances in the embedded space merely reflect relative similarities in the multidimensional parameter space. Nevertheless, the projection reveals a clear global separation between repeaters and non-repeaters, indicating that the two populations remain systematically distinct in their parameter properties even in the enlarged sam-

ple. These distributional characteristics motivate the use of objective clustering methods to further dissect the underlying populations and to obtain a more physically meaningful interpretation of the observed patterns.

To this end, we apply the Hierarchical Density-Based Spatial Clustering of Applications with Noise (HDBSCAN) algorithm (McInnes et al. 2017) to the UMAP embedded space. This method does not require a predefined number of clusters, is capable of identifying groups of arbitrary shape and size in complex distributions, and can exclude noise points. As shown in Figure 1, HDBSCAN partitions the sample into two major clusters, delineated by red and blue contours. The lower cluster contains the vast majority of confirmed repeaters,

which we designate as the Repeater-like cluster, while the upper cluster is dominated by apparent nonrepeaters, referred to as the Nonrepeater-like cluster. Notably, some degree of cross-contamination is present: the Repeater-like cluster includes a large number of FRBs that have not yet shown repetition observationally, whereas the Nonrepeater-like cluster contains a small number of confirmed repeaters.

To further facilitate an intuitive interpretation of the HDBSCAN clustering results and the UMAP embedding, and to better illustrate the characteristic differences between repeaters and non-repeaters across different classes, we randomly selected some bursts from each category and displayed their dynamic spectra (waterfall plots). These visual examples allow a direct comparison of their spectral-temporal features and overall morphology, providing complementary insight into the statistical classification results.

From the comparison of the waterfall plots of repeaters and non-repeaters shown in the lower panels of Figure 1, it is evident that the apparent non-repeaters residing within the Repeater-like cluster exhibit strong morphological similarities to confirmed repeaters. In particular, both populations predominantly display narrowband and relatively faint emission features. Such similarities suggest that these apparent non-repeaters may in fact be latent repeaters, whose subsequent bursts have not yet been detected due to limited observational exposure or instrumental sensitivity. However, as noted in [FRB Collaboration et al. \(2026\)](#), identifying genuine candidates from this population in the future will require improved localizations to rigorously exclude instrumental artifacts (e.g., grating-lobe detections) that can mimic Repeater-like features.

For repeaters that fall within the Nonrepeater-like cluster, a comparison of the waterfall plots of repeaters and non-repeaters shown in the upper panels of Figure 1 reveals that these events are predominantly characterized by broadband and comparatively brighter emission, closely resembling the spectral morphology typically associated with apparent non-repeating bursts. The presence of confirmed repeaters in the Nonrepeater-like cluster demonstrates that repeating sources can occasionally display observational properties commonly attributed to non-repeaters. Such an overlap in the high-dimensional feature space indicates that the distinction between repeaters and non-repeaters is not strictly dichotomous. Instead, it supports the interpretation that a substantial fraction—if not all—FRBs may arise from a common physical origin or represent different manifestations along an activity sequence. Hereafter, we refer to repeating bursts that fall within the Nonrepeater-like cluster as “atypical repeaters”, while those located in the Repeater-like cluster are referred to as “typical repeaters”.

Based on the UMAP projection and HDBSCAN clustering results, we can quantitatively evaluate the performance of our

unsupervised model in identifying repeating FRBs. Figure 2 presents the classification confusion matrix. Confirmed repeaters that fall within the Repeater-like cluster are regarded as successful identifications. For the full sample of 4527 FRBs, the model successfully identifies 1090 repeating bursts. The recall is defined as:

$$\text{Recall} = \frac{T_P}{T_P + F_N}, \quad (1)$$

where T_P (true positives) denotes the number of repeaters correctly classified into the Repeater-like cluster, and F_N (false negatives) represents repeaters that are incorrectly assigned to the Nonrepeater-like cluster. Based on this definition, the model achieves a recall of 0.94.

		Classified	
		Repeater	Non-Repeater
Actual	Repeater	1090	64
	Non-Repeater	1518	1855

Figure 2. Confusion matrix of the clustering classification.

This high recall rate demonstrates that the model remains exceptionally robust in capturing the fundamental high-dimensional characteristics of repeaters, even with a significantly enlarged sample size. Furthermore, the confusion matrix shows that 1518 apparent non-repeaters are assigned to the Repeater-like cluster. However, this should not be interpreted as a failure of the classification. Instead, as evidenced by their waterfall plots, these sources exhibit morphological traits—such as narrowband emission and low peak flux—that are indistinguishable from known repeaters. This aligns with the hypothesis that these events represent a population of latent repeaters or are influenced by instrumental artifacts. Consequently, the high recall and the structured distribution in the UMAP manifold confirm that our framework effectively isolates the underlying physical properties of FRB populations, providing a reliable basis for identifying repeater candidates in large-scale surveys.

Interestingly, 64 confirmed repeaters are assigned to the Nonrepeater-like cluster. In our earliest analysis based solely

on the initial CHIME/FRB dataset, we identified only a single repeating burst that was assigned to the Nonrepeater-like cluster, a result that at the time was insufficient to draw firm conclusions. As the number of detected repeating FRBs increased, our subsequent study combining the CHIME/FRB Catalog 1 with the CHIME/FRB Catalog 2023 sample (Sun et al. 2025b) revealed that a small but non-negligible subset of repeaters consistently occupied the Nonrepeater-like cluster. In that analysis, atypical repeating FRBs accounted for 4.9% of the Nonrepeater-like cluster and approximately 12% of the repeating FRB population, suggesting the possible emergence of a distinct subclass.

With the significantly expanded and more statistically robust Catalog 2 sample, we find that the absolute number of repeaters assigned to the Nonrepeater-like cluster continues to increase. However, owing to the substantial growth of the overall sample, their fractional contribution to the Nonrepeater-like cluster decreases to 3.3%, while their fraction among all repeating FRBs is measured to be 6%. Although these fractions are lower than those reported in Sun et al. (2025b), this difference is likely attributable to the limited statistical sample of repeating FRBs in the earlier analysis. Regardless, within the significantly enlarged Catalog 2 sample, the persistent occupancy of a subset of repeaters in the Nonrepeater-like cluster remains a robust result. This sustained segregation confirms the existence of a stable and distinct sub-class of repeaters whose observed characteristics are indistinguishable from typical one-off events.

To further investigate the occurrence of atypical repeating bursts across different repeating FRB sources, we analyze the fraction of atypical repeating bursts within each individual repeating source. As shown in Figure 3, out of 83 total repeater sources, 49 (55%) consistently produce “typical” repeating bursts. Conversely, the remaining 40 sources exhibit varying degrees of “atypicality”. Notably, a group of 11 sources is composed entirely of atypical bursts (atypical proportion = 1.0). While these 11 sources predominantly consist of events with low burst counts (2-3 bursts), suggesting potential statistical fluctuations, their existence highlights a population whose observed properties are indistinguishable from one-off events across their entire detected history.

This finding suggests that the traditional classification based on single-event morphology may be capturing different ‘emission modes’ rather than fundamentally different progenitors. If the majority of repeaters primarily operate in a narrowband mode but can sporadically transition into a broadband, nonrepeater-like mode, it implies a deep physical connection between the two observed populations. A more detailed comparison and analysis of the parameter differences between these two classes of repeating bursts are presented in Section 3.3.2.

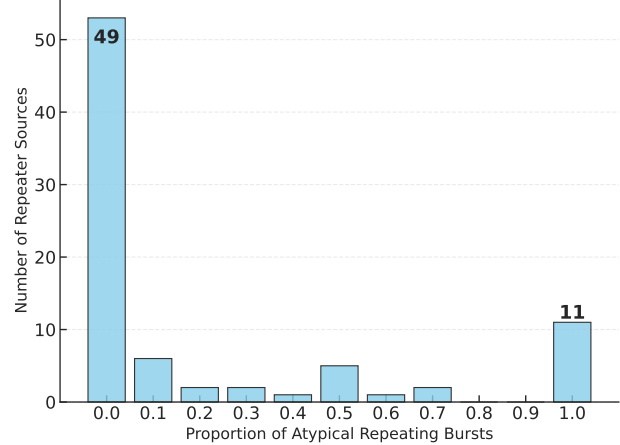


Figure 3. Distribution of the proportion of atypical repeating bursts within the repeater sources.

3.2. Feature Importance

To further elucidate the discriminative mechanism of the machine-learning model in separating repeating and non-repeating FRBs, we perform a systematic analysis of input feature importance using the SHAP (SHapley Additive ex-Planations; Lundberg & Lee 2017) method. Grounded in the Shapley value concept from game theory, SHAP quantifies the marginal contribution of each feature to the model’s output, thereby revealing its significance at both the global and individual levels. Compared to traditional feature importance metrics, SHAP provides more stable and intuitive results, specifically by differentiating how various feature values influence the prediction outcomes.

In this study, we implemented the SHAP framework in conjunction with a supervised XGBoostClassifier (Chen 2016) and calculated the SHAP value distributions for all input parameters, as shown in Figure 4. In this plot, the features are ordered along the vertical axis according to their overall importance in descending order, while the horizontal axis represents the magnitude and sign of the SHAP values, indicating the direction and strength of each feature’s contribution to the classification. The color scale, ranging from blue to red, corresponds to increasing feature values. We emphasize that, during model training, the repeater class is defined as the positive class; therefore, positive SHAP values indicate that a given feature value drives the model toward classifying an FRB as a repeater, whereas negative values imply a higher likelihood of being classified as a non-repeater.

The SHAP analysis in Figure 4 elucidates the underlying decision-making process, confirming that the parameter r remains the most dominant discriminator in the enlarged Catalog 2 sample, consistent with our prior findings (Sun et al. 2025a,b). More negative values of r tend to drive the model toward classifying FRBs as repeaters, typically corresponding to steep, narrowband bursts, whereas cases with smaller

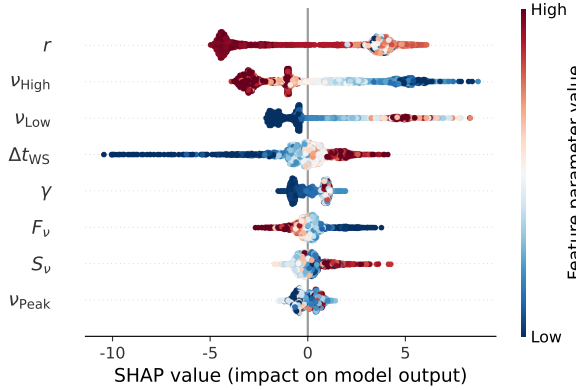


Figure 4. SHAP values for predictions in FRB classification. Features are ranked by overall importance, with the horizontal axis indicating the SHAP value, reflecting each feature’s impact on the model output.

absolute values of r are more frequently associated with non-repeaters, reflecting flatter, broadband emission. The representative waterfall plots shown in Figure 1 provide a visual validation of this pattern.

It is worth noting that the consistently dominant role of the parameter r across different datasets demonstrates the internal robustness and stability of our classification framework (Sun et al. 2025a,b). This consistency ensures that the variations in the inferred fraction of atypical repeaters under different sample selections are directly comparable, thereby lending credibility to the analysis and interpretation of their relative occurrence rates discussed above.

Beyond the spectral-morphology parameters, frequency and temporal parameters play secondary yet crucial roles. Their SHAP value distributions indicate that spectral bandwidth contributes to the classification, with lower v_{High} and higher v_{Low} (narrower bandwidth emission) being more strongly associated with repeaters. The temporal width Δt_{ws} shows a distinct bifurcated impact: larger burst widths contribute positively to repeater identification, while narrow pulses are characteristic of the Nonrepeater-like cluster. While the spectral index γ remains a theoretically important parameter, its impact in the current model appears partially overshadowed by the dominant diagnostic power of r . In contrast, flux-related parameters (F_v and S_v) as well as the peak frequency v_{Peak} show comparatively lower importance overall, though they still provide auxiliary information for classification in a subset of events. Notably, non-repeaters tend to be associated with higher values of F_v .

3.3. Parameter Distributions

In Section 3.1, the Catalog 2 sample is unsupervisedly partitioned into two primary groups through UMAP dimensionality reduction combined with the HDBSCAN clustering algorithm. Feature-importance analyses and compar-

isons of representative burst dynamic spectra indicate that this separation reflects the presence of two distinct spectral-morphological regimes within the FRB population. However, whether these regimes correspond to fundamentally different emission mechanisms remains unclear. In this section, we conduct a detailed statistical analysis of the parameter distributions to quantify and compare the observational differences between FRBs belonging to these two classes.

To investigate the intrinsic properties of FRBs, we further examine the distributions of their isotropic energy (E_{iso}), isotropic peak luminosity (L_{iso}), and brightness temperature (T_B). Because the majority of FRBs remain without host identifications and thus lack spectroscopic redshift measurements, we infer the redshift z from the dispersion measure (DM) using the catalog 2 as the basis. The total observed DM can be decomposed into several physically distinct components (Zhu-Ge et al. 2023):

$$\text{DM} = \text{DM}_{\text{MW}} + \text{DM}_{\text{Halo}} + \text{DM}_{\text{IGM}} + \frac{\text{DM}_{\text{Host}}}{1+z}, \quad (2)$$

where DM_{MW} , DM_{Halo} , DM_{IGM} , and DM_{Host} represent the respective contributions from the Milky Way interstellar medium, the Milky Way halo, the intergalactic medium, and the host galaxy of the FRB. We compute DM_{MW} using the NE2001 model (Cordes & Lazio 2002). Consequently, the extragalactic component is given by

$$\text{DM}_E = \text{DM} - \text{DM}_{\text{MW}} - \text{DM}_{\text{Halo}} = \text{DM}_{\text{IGM}} + \frac{\text{DM}_{\text{Host}}}{1+z}. \quad (3)$$

Following commonly adopted assumptions in the literature, we take $\text{DM}_{\text{Halo}} = 30 \text{ pc cm}^{-3}$ (Dolag et al. 2015; Arcus et al. 2021; Zhu-Ge et al. 2023), and adopt $\text{DM}_{\text{Host}} = 130, \text{pc cm}^{-3}$ based on recent estimates from IllustrisTNG simulations (Connor et al. 2024).

In the standard Λ CDM cosmology, the mean IGM contribution can be written as (Deng & Zhang 2014; Gao et al. 2014; Macquart et al. 2020):

$$\langle \text{DM}_{\text{IGM}}(z) \rangle = \frac{3cH_0\Omega_b}{8\pi G m_p} \int_0^z \frac{f_d(z') f_e(z') (1+z')}{\sqrt{\Omega_m(1+z')^3 + \Omega_\Lambda}} dz', \quad (4)$$

where m_p is the proton mass. The functions $f_d(z)$ and $f_e(z)$ describe the baryon mass fraction residing in the IGM and the ionized electron fraction per baryon, respectively. In this work, we adopt the recent constraints from Connor et al. (2024): $f_d = 0.93$, $f_e = 0.875$, and $\Omega_b h_{70} = 0.049$. Cosmological parameters follow the Planck2018 results, as summarized in the introduction. For sources with small DM_E , the host-galaxy contribution can exceed that of the IGM, introducing large uncertainties in the inferred redshift. To reduce this bias, our redshift estimation is restricted to FRBs with $\text{DM}_E > 160 \text{ pc cm}^{-3}$.

With the estimated redshifts, we proceed to compute E_{iso} , L_{iso} , and T_{B} for each FRB. Following Zhang (2018), E_{iso} can be written as:

$$\begin{aligned} E_{\text{iso}} &\simeq \frac{4\pi D_{\text{L}}^2}{(1+z)} F_{\text{obs}} \nu \\ &= \left(10^{39} \text{ erg}\right) \frac{4\pi}{(1+z)} \left(\frac{D_{\text{L}}}{10^{28} \text{ cm}}\right)^2 \frac{F_{\text{obs}}}{\text{Jy} \cdot \text{ms}} \frac{\nu}{\text{GHz}}, \end{aligned} \quad (5)$$

and L_{iso} is given by

$$\begin{aligned} L_{\text{iso}} &\simeq 4\pi D_{\text{L}}^2 S_{\nu,p} \nu \\ &= \left(10^{42} \text{ erg s}^{-1}\right) 4\pi \left(\frac{D_{\text{L}}}{10^{28} \text{ cm}}\right)^2 \frac{S_{\nu,p}}{\text{Jy}} \frac{\nu}{\text{GHz}}, \end{aligned} \quad (6)$$

where F_{obs} denotes the measured fluence (in units of $\text{erg cm}^{-2} \text{ Hz}^{-1}$ or $\text{Jy} \cdot \text{ms}$), $S_{\nu,p}$ is the peak flux (in units of $\text{erg s}^{-1} \text{ cm}^{-2} \text{ Hz}^{-1}$ or Jy), and D_{L} is the luminosity distance.

The brightness temperature T_{B} is calculated using the expression adopted in Petroff et al. (2019); Xiao & Dai (2022):

$$\begin{aligned} T_{\text{B}} &\simeq \frac{S_{\nu,p} D_{\text{L}}^2}{2\pi\kappa_B(\nu\Delta t)^2} \\ &= 1.1 \times 10^{35} \text{ K} \left(\frac{S_{\nu,p}}{\text{Jy}}\right) \left(\frac{D_{\text{L}}}{\text{Gpc}}\right)^2 \left(\frac{\nu}{\text{GHz}}\right)^{-2} \left(\frac{\Delta t}{\text{ms}}\right)^{-2}, \end{aligned} \quad (7)$$

where κ_B is the boltzmann constant and Δt_{ws} is the burst duration. Previous analyses (Petroff et al. 2016; Zhang 2018) typically utilized either the telescope's bandwidth B or the central frequency ν_c when evaluating E_{iso} , L_{iso} , and T_{B} . In our sample, however, a substantial fraction of bursts extends well beyond the CHIME receiver bandwidth, making these choices inappropriate. To avoid bias introduced by truncated spectra, we adopt a representative effective frequency of $\nu = 600$ MHz for bursts whose emission spans the entire band. For the subset of FRBs whose spectra lie fully within the instrumental range, we use $\nu = 400$ MHz.

In addition to the energy quantities, the parameter distribution analysis presented below incorporates the eight physical quantities selected in Section 2.2 as inputs to the UMAP projection, i.e., S_{ν} , F_{ν} , Δt_{ws} , γ , r , ν_{Low} , ν_{High} , and ν_{Peak} . We further include the frequency bandwidth $\Delta\nu$, together with three additional parameters defined in FRB Collaboration et al. (2026): the boxcar width Δt_{BW} , the scattering time Δt_{ST} , and the dispersion measure (DM), in order to provide a more comprehensive comparison of the parameter distributions among different FRB populations.

3.3.1. Parameter Comparison of Repeater-like and Nonrepeater-like Clusters

To comprehensively characterize the feature differences within the reclassified Catalog 2 sample, we temporarily

set aside the conventional repeater/non-repeater labels and instead perform a systematic comparison of the parameter distributions of FRBs belonging to the Repeater-like and Nonrepeater-like clusters. We adopt the Anderson-Darling (AD) test (Anderson & Darling 1954) to quantitatively assess the degree of statistical divergence between the two distributions. The AD test evaluates the null hypothesis that the two samples are drawn from the same parent population. A p -value smaller than 0.05 leads to rejection of the null hypothesis, indicating a statistically significant difference between the Repeater-like and Nonrepeater-like clusters. Figure 5 presents the resulting distributions together with the corresponding AD test statistics. In particular, $p_{\text{AD}} \leq 0.001$ indicates extremely significant differences across the examined parameters, while the normalized test statistic s_{AD} provides a direct measure of the strength of the distributional separation.

As shown in Figure 5, a global comparison reveals that the Repeater-like cluster (red) and the Nonrepeater-like cluster (blue) exhibit statistically significant differences across all examined physical parameters ($p_{\text{AD}} \leq 0.001$). The most pronounced separation arises from the spectral-morphology parameters r ($s_{\text{AD}} = 2047.55$) and γ ($s_{\text{AD}} = 1703.40$), whose exceptionally large normalized AD statistics demonstrate that these two parameters play a dominant role in driving the segregation observed in the high-dimensional feature space.

The parameter r characterizes the curvature of the emission spectrum around the central frequency and is therefore directly linked to the effective emission bandwidth. Values of $r \sim 0$ correspond to relatively flat, broadband spectra, whereas $r < 0$ indicates pronounced narrowband emission. We find that FRBs in the Nonrepeater-like cluster predominantly concentrate around $r \sim 0$, consistent with broadband spectral characteristics. In contrast, the Repeater-like cluster preferentially occupies the $r < 0$ region, exhibiting significantly narrower spectral features. This behavior is fully consistent with the distribution of the frequency bandwidth $\Delta\nu$, reinforcing the conclusion that the two clusters differ systematically in their spectral morphology.

Regarding temporal characteristics, FRBs in the Repeater-like cluster display systematically longer pulse widths Δt_{ws} than those in the Nonrepeater-like cluster ($s_{\text{AD}} = 193.34$). Taken together, the combination of longer durations and narrower bandwidths constitutes a robust observational signature of the Repeater-like population. This coherent set of properties naturally explains the high degree of clustering and clear separation of this population in the UMAP embedding space.

In addition, the Nonrepeater-like cluster systematically exhibits higher values of S_{ν} and F_{ν} , revealing a clear distinction between the two populations in their radiative energy scales. To more directly assess differences in radiative intensity and emission efficiency, we further compare the mean values of E_{iso} , L_{iso} , and T_{B} between the two clusters.

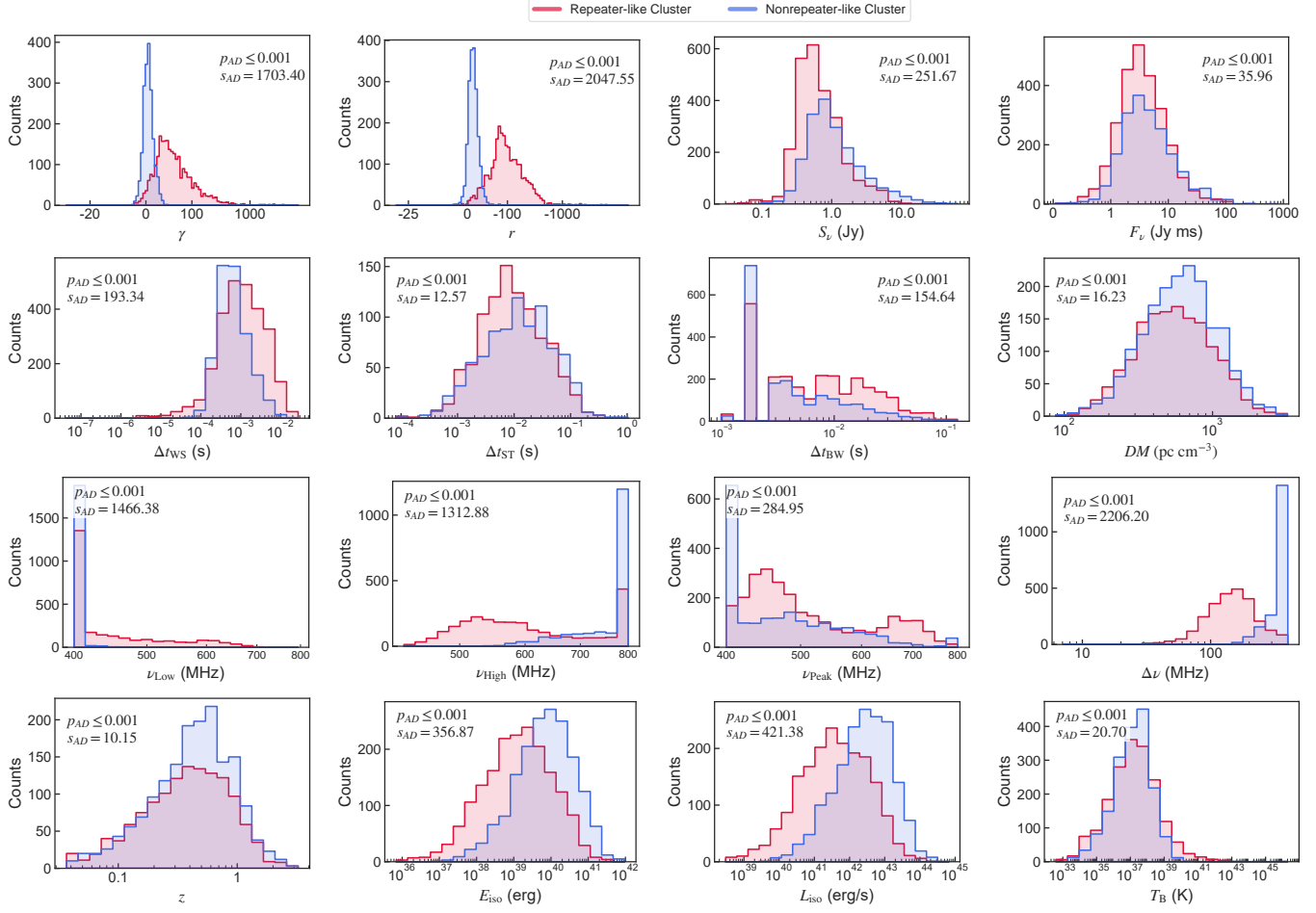


Figure 5. Parameter distribution comparison between the Repeater-like and Nonrepeater-like clusters. The p_{AD} and s_{AD} values in each panel denote the p -value and test statistic of the AD test, respectively, indicating the statistical significance of the distributional differences between the two clusters.

As summarized in Table 1, the Nonrepeater-like cluster displays substantially higher mean values of E_{iso} (2.51×10^{40} erg) and L_{iso} (9.80×10^{42} erg s $^{-1}$) compared to the Repeater-like cluster, whose corresponding mean energy and luminosity are 7.50×10^{39} erg and 2.75×10^{42} erg s $^{-1}$, respectively. This pronounced difference in the mean values indicates that Nonrepeater-like FRBs typically release more energetic bursts, whereas Repeater-like FRBs tend to exhibit frequent activity at comparatively lower energy levels.

Notably, the Nonrepeater-like cluster exhibits slightly higher dispersion measures and redshifts than the Repeater-like cluster. The physical origin of this difference remains unclear; a more plausible explanation is that it arises from observational selection effects. At higher redshifts, only intrinsically energetic and luminous bursts are detectable, whereas the fainter, lower-energy bursts characteristic of repeating FRBs are more likely to fall below the detection threshold at large distances.

Table 1. The comparison of mean values and distributions of FRB intrinsic property parameters.

Sample Type	$\log_{10} E_{\text{iso}}$ (erg)	$\log_{10} L_{\text{iso}}$ (erg s $^{-1}$)	$\log_{10} T_{\text{B}}$ (K)	z
Repeater-like cluster	39.88	42.44	40.33	0.44
Nonrepeater-like cluster	40.40	42.99	38.25	0.53
Typical repeaters	39.69	41.92	38.03	0.28
Atypical repeaters	40.26	42.56	37.42	0.32

Taken together, the parameter-distribution comparisons and AD test results indicate that the Repeater-like cluster captures a physically coherent bursting mode within the FRB population, characterized by narrowband emission and lower radiated energies, whereas the Nonrepeater-like cluster represents a broadband, high-energy emission mode. This dichotomy suggests that the underlying burst-triggering mechanisms of the two populations differ significantly in their efficiency of energy release (Kirsten et al. 2024).

3.3.2. Parameter Comparison of Typical repeaters and Atypical repeaters

During the UMAP reduction of the Catalog 2, we find that FRBs originating from repeating sources do not concentrate into a single cluster in the embedding space. Instead, they are separated into two distinct clusters, indicating the presence of systematic heterogeneity within repeating bursts themselves. Motivated by this result, we further divide repeating bursts into typical repeaters, defined as repeating FRBs that reside within the Repeater-like cluster, and atypical repeaters, defined as repeating FRBs that are located within the Nonrepeater-like cluster. This classification does not reflect differences between sources, but rather a statistical separation occurring within individual repeating sources. Atypical repeating bursts typically appear only sporadically within the burst sequences of repeating sources, yet they exhibit properties that are markedly distinct from those of the majority of typical repeating bursts. Figure 6 presents the distributions of key physical parameters for these two classes, together with the corresponding AD test results, where the red stepped lines represent typical repeaters and the orange stepped lines denote atypical repeaters.

As illustrated in Figure 6, typical and atypical repeating bursts exhibit systematic differences across multiple parameter dimensions. The most pronounced contrasts arise in the spectral parameters r and γ . Typical repeaters predominantly occupy the region characterized by $\gamma > 0$ and $r < 0$, indicative of steep spectral profiles and pronounced narrowband emission. In contrast, atypical repeating bursts preferentially populate the $\gamma \leq 0$ and $r \geq 0$ regime, displaying flatter spectral shapes and broadband emission properties that closely resemble those of apparent one-off events. The AD test quantitatively confirms these distinctions, yielding normalized test statistics of $s_{\text{AD}} = 192.61$ for γ and $s_{\text{AD}} = 145.93$ for r , thereby demonstrating an intrinsic separability between the two classes in spectral-morphology parameter space.

In terms of temporal properties, typical repeaters exhibit longer pulse durations, as quantified by Δt_{ws} , whereas atypical repeating bursts tend to be shorter. This behavior is fully consistent with trends previously reported in comparisons between repeating and non-repeating FRBs (Scholz et al. 2016; CHIME/FRB Collaboration et al. 2019; Fonseca et al. 2020; CHIME/FRB Collaboration et al. 2021; Zhong et al. 2022; CHIME/FRB Collaboration et al. 2023).

In addition, atypical repeating bursts tend to exhibit higher flux densities, implying a stronger radiative output. We further compare the mean values of E_{iso} , L_{iso} , and T_{B} between the two populations, with the results summarized in Table 1. The mean energy and luminosity of atypical repeating bursts (1.83×10^{40} erg; 3.66×10^{42} erg s $^{-1}$) are markedly higher than those of typical repeaters (4.85×10^{39} erg; 8.25×10^{41} erg s $^{-1}$). This result provides strong evidence that, when a

repeating source produces atypical bursts, the scale of energy release is significantly enhanced, exceeding the characteristic energy range of typical repeating activity and entering a high-energy regime comparable to that of apparent non-repeating bursts.

Notably, the mean brightness temperature of atypical repeating bursts (2.62×10^{37} K) is slightly lower than that of typical repeaters (1.08×10^{38} K). This combination of higher energy yet lower brightness temperature may indicate a reduced radiative coherence efficiency in the atypical bursting mode relative to the typical narrowband repeating mode. In addition, although the AD test yields a p -value of 0.046 for the redshift distributions-formally below the 0.05 threshold-the overall difference remains marginal.

Taken together, the presence of atypical repeating bursts indicates that repeating FRB sources do not operate under a single, fixed radiative mode. These atypical events exhibit observational properties-such as bandwidth, energy scale, and temporal structure-that closely resemble those of apparently non-repeating bursts, thereby obscuring their repeating nature at the level of individual bursts. This suggests that some repeating sources may temporarily enter a radiative state characterized by higher energies and broader bandwidths, leading to an overlap with non-repeating bursts in the observed parameter space. Such behavior blurs the traditional phenomenological distinction between repeating and non-repeating FRBs, implying that the two populations may not be fundamentally distinct in their emission physics, but instead share similar underlying mechanisms that differ primarily in activity level, energy-release behavior, or occurrence rate.

It should be emphasized that the current sample of repeating sources remains limited, making it difficult to determine whether atypical repeating bursts correspond to a specific source state or merely reflect transitions between emission modes. Future observations of a larger population of repeating sources will allow for more robust and detailed tests of these differences and their underlying physical origins.

4. CONCLUSION

In this work, we analyze the multi-dimensional observational properties of FRBs using the largest homogeneous sample Catalog 2. We adopt an unsupervised machine learning framework that combines UMAP with HDBSCAN clustering to reclassify 4527 burst events. The method remains stable in the large-sample regime, achieving a recall of 0.94 for known repeating sources, and enables a systematic comparison of the statistical properties of different FRB clusters. We have the following findings.

1. Based on an unsupervised analysis of the Catalog 2, we find that FRBs exhibit a clear and stable structural separation in the embedding space, primarily dividing into two statistically significant clusters. The Repeater-

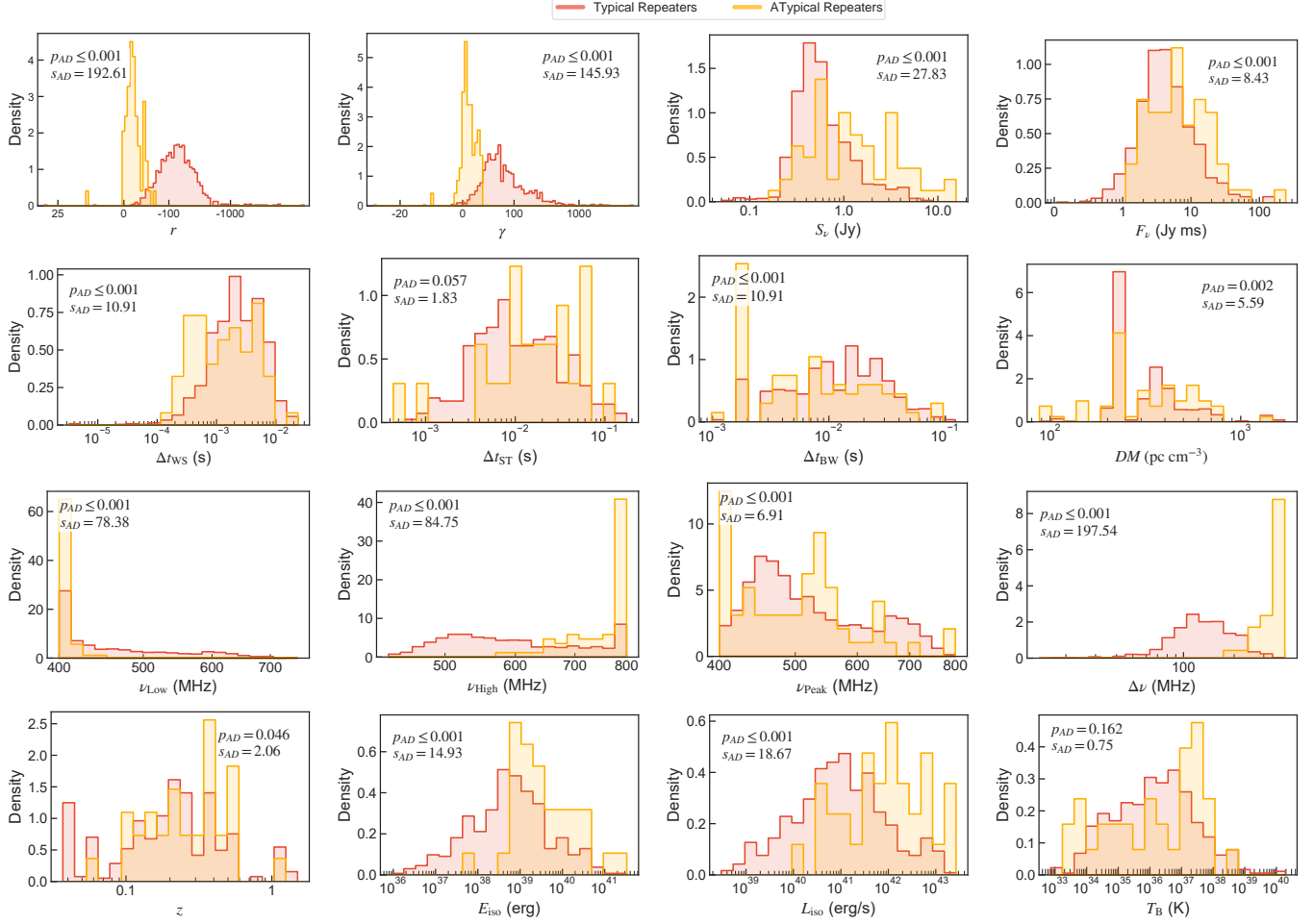


Figure 6. Parameter distribution comparisons between typical repeaters and atypical repeaters. The p_{AD} and s_{AD} values denote the results of the AD test for each parameter.

like cluster is characterized by narrowband emission and longer pulse widths, encompassing the majority of known repeating bursts, whereas the Nonrepeater-like cluster displays broadband, high-energy, and short-timescale properties. This separation is consistently reflected in both the UMAP low-dimensional representation and the observed dynamic spectra, demonstrating the strong physical interpretability of the classification.

2. Feature-importance analysis shows that the spectral morphology parameter, spectral running (r), consistently serves as the most discriminating metric between repeating and non-repeating FRBs, reflecting a fundamental difference in their emission bandwidths. This result further indicates that narrowband emission is an intrinsic and stable radiative property of the repeating FRB population.
3. With support from large-sample statistics, we identify a robust subclass of atypical repeaters, accounting

for approximately $\sim 6\%$ of the repeating FRB population. Although these events originate from known repeating sources, they occupy the same region of the multi-dimensional parameter space as non-repeating bursts, exhibiting broadband, short-timescale, and high-energy characteristics, while showing statistically significant differences from the typical repeating bursts produced by the same sources. This result indicates that a single FRB source can exhibit multiple emission modes, thereby blurring the observational boundary between repeating and non-repeating FRBs.

4. A statistical comparison between the Repeater-like and Nonrepeater-like clusters shows that the latter exhibits systematically higher redshifts, larger E_{iso} , and higher L_{iso} . These systematic differences are consistent with a scenario in which some apparently non-repeating FRBs arise from observational incompleteness, such that observations preferentially capture sources during

high-energy activity states, while lower-energy repeating bursts remain undetected due to limited sensitivity.

By leveraging the Catalog 2 sample and its multi-dimensional observational parameters within an unsupervised machine learning framework, this study effectively reveals the natural clustering structure of the FRB population and the presence of potential subpopulations. As the FRB sample size continues to grow, the boundary between repeating and non-repeating sources appears increasingly blurred, with the identification of atypical repeaters providing strong evidence for physical continuity or a shared origin between the two populations.

ACKNOWLEDGMENTS

We acknowledge the support of the National Natural Science Foundation of China (Grants Nos. 12473001, 12533001, and 12575049), the National SKA Program of China (Grant Nos. 2022SKA0110200, 2022SKA0110203), the China Manned Space Program (Grant No. CMS-CSST-2025-A02), and the National 111 Project (Grant No. B16009). Y.L. acknowledges the support of the National Natural Science Foundation of China (No.12473091). F.-W.Z. acknowledges the support from the National Natural Science Foundation of China (No. 12463008) and the Guangxi Natural Science Foundation (No. 2022GXNSFDA035083). Yong-Kun Zhang is supported by the Postdoctoral Fellowship Program and China Postdoctoral Science Foundation (Grant Number BX20250158).

REFERENCES

Aghanim, N., et al. 2020, *Astron. Astrophys.*, 641, A6, doi: [10.1051/0004-6361/201833910](https://doi.org/10.1051/0004-6361/201833910)

Anderson, T. W., & Darling, D. A. 1954, *Journal of the American statistical association*, 49, 765

Arcus, W. R., Macquart, J. P., Sammons, M. W., James, C. W., & Ekers, R. D. 2021, *MNRAS*, 501, 5319, doi: [10.1093/mnras/staa3948](https://doi.org/10.1093/mnras/staa3948)

Arni, R., Blanco, C., & Prabhu, A. 2025, arXiv e-prints, arXiv:2511.02634, doi: [10.48550/arXiv.2511.02634](https://doi.org/10.48550/arXiv.2511.02634)

Becht, E., McInnes, L., Healy, J., et al. 2019, *Nature biotechnology*, 37, 38

Bochenek, C. D., Ravi, V., Belov, K. V., et al. 2020, *Nature*, 587, 59, doi: [10.1038/s41586-020-2872-x](https://doi.org/10.1038/s41586-020-2872-x)

Brown, K., Chamma, M. A., Rajabi, F., et al. 2024, *MNRAS*, 529, L152, doi: [10.1093/mnrasl/slae012](https://doi.org/10.1093/mnrasl/slae012)

Chen, B. H., Hashimoto, T., Goto, T., et al. 2022, *MNRAS*, 509, 1227, doi: [10.1093/mnras/stab2994](https://doi.org/10.1093/mnras/stab2994)

Chen, T. 2016, Cornell University

CHIME/FRB Collaboration, Andersen, B. C., Bandura, K., et al. 2019, *ApJL*, 885, L24, doi: [10.3847/2041-8213/ab4a80](https://doi.org/10.3847/2041-8213/ab4a80)

CHIME/FRB Collaboration, Andersen, B. C., Bandura, K. M., et al. 2020, *Nature*, 587, 54, doi: [10.1038/s41586-020-2863-y](https://doi.org/10.1038/s41586-020-2863-y)

CHIME/FRB Collaboration, Amiri, M., Andersen, B. C., et al. 2021, *ApJS*, 257, 59, doi: [10.3847/1538-4365/ac33ab](https://doi.org/10.3847/1538-4365/ac33ab)

CHIME/FRB Collaboration, Andersen, B. C., Bandura, K., et al. 2023, *ApJ*, 947, 83, doi: [10.3847/1538-4357/acc6c1](https://doi.org/10.3847/1538-4357/acc6c1)

CHIME/FRB Collaboration, Abbott, T. C., Amouyal, D., et al. 2025, *ApJL*, 989, L48, doi: [10.3847/2041-8213/adf62f](https://doi.org/10.3847/2041-8213/adf62f)

Connor, L., Ravi, V., Sharma, K., et al. 2024, arXiv e-prints, arXiv:2409.16952, doi: [10.48550/arXiv.2409.16952](https://doi.org/10.48550/arXiv.2409.16952)

Cordes, J. M., & Lazio, T. J. W. 2002, arXiv e-prints, astro, doi: [10.48550/arXiv.astro-ph/0207156](https://doi.org/10.48550/arXiv.astro-ph/0207156)

Cui, X.-H., Zhang, C.-M., Wang, S.-Q., et al. 2021, *MNRAS*, 500, 3275, doi: [10.1093/mnras/staa3351](https://doi.org/10.1093/mnras/staa3351)

Deng, W., & Zhang, B. 2014, *ApJL*, 783, L35, doi: [10.1088/2041-8205/783/2/L35](https://doi.org/10.1088/2041-8205/783/2/L35)

Dolag, K., Gaensler, B. M., Beck, A. M., & Beck, M. C. 2015, *MNRAS*, 451, 4277, doi: [10.1093/mnras/stv1190](https://doi.org/10.1093/mnras/stv1190)

Fonseca, E., Andersen, B. C., Bhardwaj, M., et al. 2020, *ApJL*, 891, L6, doi: [10.3847/2041-8213/ab7208](https://doi.org/10.3847/2041-8213/ab7208)

FRB Collaboration, Abbott, T., Andersen, B. C., et al. 2026, arXiv e-prints, arXiv:2601.09399, doi: [10.48550/arXiv.2601.09399](https://doi.org/10.48550/arXiv.2601.09399)

Gao, H., Li, Z., & Zhang, B. 2014, *ApJ*, 788, 189, doi: [10.1088/0004-637X/788/2/189](https://doi.org/10.1088/0004-637X/788/2/189)

García, C. R., Torres, D. F., Zhu-Ge, J.-M., & Zhang, B. 2024, *ApJ*, 977, 273, doi: [10.3847/1538-4357/ad9020](https://doi.org/10.3847/1538-4357/ad9020)

Júnior, A. J. B., Fortunato, J. A. S., Silvestre, L. J., Alencar, T. V., & Hipólito-Ricaldi, W. S. 2026, *Journal of High Energy Astrophysics*, 49, 100449, doi: [10.1016/j.jheap.2025.100449](https://doi.org/10.1016/j.jheap.2025.100449)

Kharel, B., Fonseca, E., Brar, C., et al. 2025, <https://arxiv.org/abs/2509.06208>

Kharel, B., Fonseca, E., Brar, C., et al. 2025, arXiv e-prints, arXiv:2509.06208, doi: [10.48550/arXiv.2509.06208](https://doi.org/10.48550/arXiv.2509.06208)

Kirsten, F., Ould-Boukattine, O. S., Herrmann, W., et al. 2024, *Nature Astronomy*, 8, 337, doi: [10.1038/s41550-023-02153-z](https://doi.org/10.1038/s41550-023-02153-z)

Kumar, P., Shannon, R. M., Flynn, C., et al. 2021, *MNRAS*, 500, 2525, doi: [10.1093/mnras/staa3436](https://doi.org/10.1093/mnras/staa3436)

Liu, L., Lin, H.-N., & Tang, L. 2025, *Chinese Physics C*, doi: [10.1088/1674-1137/ae0725](https://doi.org/10.1088/1674-1137/ae0725)

Lorimer, D. R., Bailes, M., McLaughlin, M. A., Narkevic, D. J., & Crawford, F. 2007, *Science*, 318, 777, doi: [10.1126/science.1147532](https://doi.org/10.1126/science.1147532)

Lundberg, S. M., & Lee, S.-I. 2017, 30, https://proceedings.neurips.cc/paper_files/paper/2017/file/8a20a8621978632d76c43dfd28b67767-Paper.pdf

Luo, J.-W., Zhu-Ge, J.-M., & Zhang, B. 2023, MNRAS, 518, 1629, doi: [10.1093/mnras/stac3206](https://doi.org/10.1093/mnras/stac3206)

Ma, W. Q., Gao, Z. F., Li, B. P., et al. 2025, ApJ, 981, 24, doi: [10.3847/1538-4357/adaf19](https://doi.org/10.3847/1538-4357/adaf19)

Macquart, J. P., Prochaska, J. X., McQuinn, M., et al. 2020, Nature, 581, 391, doi: [10.1038/s41586-020-2300-2](https://doi.org/10.1038/s41586-020-2300-2)

Madheshwaran, M., Hashimoto, T., Goto, T., et al. 2025, PASP, 137, 124102, doi: [10.1088/1538-3873/ae215b](https://doi.org/10.1088/1538-3873/ae215b)

Marcote, B., Paragi, Z., Hessels, J. W. T., et al. 2017, ApJL, 834, L8, doi: [10.3847/2041-8213/834/2/L8](https://doi.org/10.3847/2041-8213/834/2/L8)

McInnes, L., Healy, J., & Astels, S. 2017, JOSS, 2, 205, doi: [10.21105/joss.00205](https://doi.org/10.21105/joss.00205)

McInnes, L., Healy, J., & Melville, J. 2018. <https://arxiv.org/abs/1802.03426>

Ould-Boukattine, O. S., Chawla, P., Hessels, J. W. T., et al. 2024, arXiv e-prints, arXiv:2410.17024, doi: [10.48550/arXiv.2410.17024](https://doi.org/10.48550/arXiv.2410.17024)

Pastor-Marazuela, I., Gordon, A. C., Stappers, B., et al. 2026, MNRAS, 545, staf2144, doi: [10.1093/mnras/staf2144](https://doi.org/10.1093/mnras/staf2144)

Petroff, E., Hessels, J. W. T., & Lorimer, D. R. 2019, A&A Rv, 27, 4, doi: [10.1007/s00159-019-0116-6](https://doi.org/10.1007/s00159-019-0116-6)

Petroff, E., Hessels, J. W. T., & Lorimer, D. R. 2022, A&A, 30, doi: [10.1007/s00159-022-00139-w](https://doi.org/10.1007/s00159-022-00139-w)

Petroff, E., Barr, E. D., Jameson, A., et al. 2016, PASA, 33, e045, doi: [10.1017/pasa.2016.35](https://doi.org/10.1017/pasa.2016.35)

Pleunis, Z., Good, D. C., Kaspi, V. M., et al. 2021, ApJ, 923, 1, doi: [10.3847/1538-4357/ac33ac](https://doi.org/10.3847/1538-4357/ac33ac)

Qiang, D.-C., Zheng, J., You, Z.-Q., & Yang, S. 2025, ApJ, 982, 16, doi: [10.3847/1538-4357/adb72b](https://doi.org/10.3847/1538-4357/adb72b)

Scholz, P., Spitler, L. G., Hessels, J. W. T., et al. 2016, ApJ, 833, 177, doi: [10.3847/1538-4357/833/2/177](https://doi.org/10.3847/1538-4357/833/2/177)

Sharma, A., & Rajpaul, V. M. 2024, MNRAS, 533, 3283, doi: [10.1093/mnras/stae1972](https://doi.org/10.1093/mnras/stae1972)

Sheikh, S. Z., Farah, W., Pollak, A. W., et al. 2024, MNRAS, 527, 10425, doi: [10.1093/mnras/stad3630](https://doi.org/10.1093/mnras/stad3630)

Spitler, L. G., Cordes, J. M., Hessels, J. W. T., et al. 2014, ApJ, 790, 101, doi: [10.1088/0004-637X/790/2/101](https://doi.org/10.1088/0004-637X/790/2/101)

Sun, W.-P., Zhang, J.-G., Li, Y., et al. 2025a, ApJ, 980, 185, doi: [10.3847/1538-4357/adad6a](https://doi.org/10.3847/1538-4357/adad6a)

Sun, W.-P., Zhang, Y.-K., Zhang, J.-G., et al. 2025b, arXiv e-prints, arXiv:2510.16338, doi: [10.48550/arXiv.2510.16338](https://doi.org/10.48550/arXiv.2510.16338)

Tendulkar, S. P., Bassa, C. G., Cordes, J. M., et al. 2017, ApJL, 834, L7, doi: [10.3847/2041-8213/834/2/L7](https://doi.org/10.3847/2041-8213/834/2/L7)

Thornton, D., Stappers, B., Bailes, M., et al. 2013, Science, 341, 53, doi: [10.1126/science.1236789](https://doi.org/10.1126/science.1236789)

Xiao, D., & Dai, Z.-G. 2022, A&A, 657, L7, doi: [10.1051/0004-6361/202142268](https://doi.org/10.1051/0004-6361/202142268)

Yang, X., Zhang, S. B., Wang, J. S., & Wu, X. F. 2023, MNRAS, 522, 4342, doi: [10.1093/mnras/stad1304](https://doi.org/10.1093/mnras/stad1304)

Zhang, B. 2018, ApJL, 867, L21, doi: [10.3847/2041-8213/aae8e3](https://doi.org/10.3847/2041-8213/aae8e3)

Zhang, B. 2023, RMP, 95, doi: [10.1103/revmodphys.95.035005](https://doi.org/10.1103/revmodphys.95.035005)

Zhang, B. 2024, Annual Review of Nuclear and Particle Science, 74, 89, doi: [10.1146/annurev-nucl-102020-124444](https://doi.org/10.1146/annurev-nucl-102020-124444)

Zhang, J.-G., Jiang, Y.-F., Zhao, Z.-W., et al. 2025a, Science China Physics, Mechanics, and Astronomy, 68, 280406, doi: [10.1007/s11433-024-2647-2](https://doi.org/10.1007/s11433-024-2647-2)

Zhang, J.-G., Song, J.-Y., Zhao, Z.-W., et al. 2025b, arXiv e-prints, arXiv:2507.06841, doi: [10.48550/arXiv.2507.06841](https://doi.org/10.48550/arXiv.2507.06841)

Zhang, J.-G., Zhao, Z.-W., Li, Y., et al. 2023, Science China Physics, Mechanics, and Astronomy, 66, 120412, doi: [10.1007/s11433-023-2212-9](https://doi.org/10.1007/s11433-023-2212-9)

Zhang, K., Li, L., Zhang, Z., et al. 2022, Universe, 8, 355, doi: [10.3390/universe8070355](https://doi.org/10.3390/universe8070355)

Zhao, Z.-W., Li, Z.-X., Qi, J.-Z., et al. 2020, ApJ, 903, 83, doi: [10.3847/1538-4357/abb8ce](https://doi.org/10.3847/1538-4357/abb8ce)

Zhong, S.-Q., Xie, W.-J., Deng, C.-M., et al. 2022, ApJ, 926, 206, doi: [10.3847/1538-4357/ac4d98](https://doi.org/10.3847/1538-4357/ac4d98)

Zhu-Ge, J.-M., Luo, J.-W., & Zhang, B. 2023, MNRAS, 519, 1823, doi: [10.1093/mnras/stac3599](https://doi.org/10.1093/mnras/stac3599)